

# LABORATORY MEASUREMENTS AND MODELING OF THE Fe xvii X-RAY SPECTRUM

G. V. BROWN,<sup>1</sup> P. BEIERSDORFER, D. A. LIEHAHL, AND K. WIDMANN

Department of Physics and Space Technology, Lawrence Livermore National Laboratory, 7000 East Avenue, Livermore, CA 94551

AND

S. M. KAHN

Department of Physics and Columbia Astrophysics Laboratory, Columbia University, New York, NY 10027

Received 1997 November 19; accepted 1998 March 6

## ABSTRACT

Detailed measurements, line identifications, and modeling calculations of the Fe xvii L-shell emission spectrum between 9.8 and 17.5 Å are presented. The measurements were carried out on an electron beam ion trap under precisely controlled conditions where electron-impact excitation followed by radiative cascades is the dominant line formation process. In addition to the strong transitions emanating from the  $n = 3$  shell, we identify and accurately determine wavelengths for transitions from higher shells up to  $n = 11$ , including two electric quadrupole transitions that have not been previously identified. Various theoretical values, including new distorted wave calculations, are compared to our measurements, which establish definitive values for testing spectral modeling predictions. We find a value of  $3.04 \pm 0.12$  for the ratio of the intensity of the  $2p-3d^1P_1$  resonance and of the  $2p-3d^3D_1$  intercombination line situated at 15.01 and 15.26 Å, respectively. This value is higher than the values observed in solar spectra, which supports claims that the solar value is affected by resonant scattering. However, because our value is significantly lower than calculated values, the amount of scattering has probably been overestimated in past analyses. Comparisons of the measured intensity ratios of the transitions originating in levels of higher principal quantum number  $n$  with present distorted wave calculations show good agreement up to  $n = 6$ . The combined flux of all  $2p-nd$  transitions with  $n \geq 5$  and all  $2s-np$  transitions with  $n = 4$  and 5 relative to the flux of the 15.01 Å resonance line has been measured to be  $0.13^{+0.04}_{-0.03}$ .

*Subject headings:* atomic data — atomic processes — line: identification — Sun: X-rays, gamma rays — X-rays: general

## 1. INTRODUCTION

Fe xvii is the dominant Fe ion over a broad temperature range in coronal equilibrium (Arnaud & Raymond 1992; Arnaud & Rothenflug 1985) whose intense X-ray emission has been observed in a wide range of astrophysical sources. In particular, L-shell emission from Fe xvii, which falls between 9.8 and 17.5 Å, has been observed in supernova remnants (Winkler et al. 1981), solar active regions (Blake et al. 1965; Freeman & Jones 1970; Parkinson 1975; Hutcheon, Pye, & Evans 1976; McKenzie et al. 1980; Phillips et al. 1982; Waljeski et al. 1994), stellar coronae (Vedder & Canizares 1983), and X-ray binaries (Kahn, Seward & Chlebowski 1984). Because of the abundance of sources, Fe xvii L-shell emission has been extensively studied in order to fully exploit its diagnostic potential. In the case of the Sun, comparisons of Fe xvii L-shell emission with theoretical modeling calculations have suggested its utility as a diagnostic of density (Schmelz, Saba, & Strong 1992; Waljeski et al. 1994; Phillips et al. 1996), temperature (Raymond & Smith 1986), ion abundance (Waljeski et al. 1994), and the dimensions of active regions of the Sun (Phillips et al. 1996; Waljeski et al. 1994). Also, the flux of the iron L-complex has been used to estimate the iron abundance in low-temperature regions of elliptical galaxies (Arimoto et al. 1997; Hwang et al. 1997).

The utility of Fe xvii lines as plasma diagnostics depends critically on the accuracy of atomic models used to interpret the spectra. Unfortunately, the models that have been available to date do not always agree on the predicted intensities

of the most prominent transitions, e.g.,  $2p^5 3d_{3/2}^1 P_1 \rightarrow 2p^6 {}^1 S_0$ ,  $2p^5 3d_{5/2}^3 D_1 \rightarrow 2p^6 {}^1 S_0$ ,  $2p^5 3s_{1/2}^1 P_1 \rightarrow 2p^6 {}^1 S_0$ , and  $2p^5 3s_{1/2}^3 P_1 \rightarrow 2p^6 {}^1 S_0$ , which lie at 15.01, 15.26, 16.78, and 17.05 Å, respectively (Cornille et al. 1994; Bhatia & Doschek 1992; Hagelstein & Jung 1987; Louergue & Nussbaumer 1975). In particular, in the case of the lines connecting the upper levels  $2p^5 3d_{3/2}^1 P_1$  and  $2p^5 3d_{5/2}^3 D_1$  to the  $2p^6 {}^1 S_0$  ground state (hereafter  $\lambda 15.01$  and  $\lambda 15.26$ , respectively), the predicted intensity ratio,  $I(\lambda 15.01)/I(\lambda 15.26)$ , varies from 2.7 to 4.5 (Cornille et al. 1994; Waljeski et al. 1994; Bhatia & Doschek 1992; Louergue & Nussbaumer 1975). Moreover, there are large discrepancies between the calculated intensities and those observed in the Sun, which range from 1.60 to 2.7 (Waljeski et al. 1994; McKenzie et al. 1980; Hutcheon et al. 1976; Parkinson 1975; Blake et al. 1965). The discrepancy has been attributed to resonant scattering (Waljeski et al. 1994; Schmelz et al. 1992; Rugge & McKenzie 1985). In the absence of a laboratory confirmation of any one of the theoretical values for these line intensities, the validity of the inferred astrophysical conditions remains doubtful.

The  $n = 3 \rightarrow n = 2$  lines, which dominate the L-shell emission spectrum of Fe xvii, have received the most attention in both laboratory and solar measurements. First identified in vacuum spark plasmas (Tyrén 1938), L-shell emission from iron has been observed in exploding wires (Burkhalter et al. 1978), laser-produced plasmas (Boiko, Faenov, & Pikuz 1978), and tokamaks (von Goeler et al. 1982). In these laboratory sources, most excitation processes, such as dielectronic recombination, charge exchange, inner shell ionization, high-density collisional depopulation and mixing, and electron-impact excitation, take place simultaneously. The interpretation of these laboratory

<sup>1</sup> Also at 206 Allison Lab, Auburn University Physics Department, Auburn University, AL 36849.

spectra, as for solar spectra, thus depend on the proper modeling of the charge balance and the correct mix of line formation processes, and in many cases a true test of the fundamental atomic physics entering the spectral modeling calculation is precluded.

Fe xvii emission from levels with  $n \geq 4$  is weaker than that from  $n = 3$  and has received less attention. Lines from levels up to  $n = 6$  have been identified in solar observations (Phillips et al. 1982), while lines from levels up to  $n = 7$  have been identified in laboratory observations (Boiko et al. 1978). Because the high- $n$  lines are relatively weak, they may easily “disappear” in blends with lines of the higher charge states of iron that are situated in the wavelength region from 10 to 13 Å. Reliable identification, wavelength assignments, and intensity information related to the high- $n$  transitions of Fe xvii are needed to interpret the spectra and to account for all of the flux contained in this region as well as to provide important tests of calculational capabilities.

Here, we present measurements of the emission lines in Fe xvii of the type  $n \rightarrow 2$  with  $3 \leq n \leq 11$ . These measurements represent a complete set of Fe xvii emission in a low-density plasma at electron energies above threshold, i.e., these lines contain all of the significant flux from Fe xvii emitted in the soft X-ray region due to direct impact excitation and radiative cascades and provide both accurate line positions and intensities. The measurements were performed under well-controlled laboratory conditions using the Electron Beam Ion Trap (EBIT) located at the Lawrence Livermore National Laboratory. This source employs a monoenergetic electron beam to produce a single charge state and to select the excitation process of interest. The present measurements were made at beam energies at which the only excitation process is electron-impact excitation followed by subsequent radiative cascades. Because the electron density of this source is low ( $n_e \approx 10^{12} \text{ cm}^{-3}$ ), high-density collisional or opacity related effects can be neglected, unlike most other laboratory sources. The measurements thus allowed us not only to identify lines that have not been identified before, including two electric quadrupole transitions, and to determine their wavelengths with high accuracy but also to determine the relative intensities of many of the lines. These line identifications and relative line intensities can be used to test modeling calculations and the underlying atomic physics on which the models are based. This will provide important validation for the use of the iron L-shell emission features to diagnose physical conditions in astrophysical plasmas using high-resolution spectra that will be collected with upcoming missions, such as the *X-ray Multi-Mirror* mission and the *Advanced X-ray Astrophysics Facility*.

## 2. EXPERIMENTAL SETUP

The present measurement was conducted on the EBIT facility located at the Lawrence Livermore National Laboratory. EBIT, which was specifically designed for the creation and study of highly charged ions (Levine et al. 1988), consists of an electron beam, an electrostatic trapping region in which ion-electron interactions take place, a collector in which the beam is collected after interaction, and a metal vacuum vapor arc (MeVVA) used for injection of the target ions. The MeVVA produces singly or doubly ionized ions that are injected into the trap and further ionized to the desired charge state collisionally by the electron beam. The trap is emptied and filled with new ions every second to

prevent any appreciable accumulation of background ions from other sources, such as tungsten from the electron gun filament. The source has already provided detailed tests of K-shell atomic data (Chantrenne et al. 1992; Beiersdorfer et al. 1992; Wargelin, Beiersdorfer, & Kahn 1993; Decaux et al. 1995; Decaux et al. 1997). Detailed tests of L-shell spectra have now been made possible by the development of suitable spectrometers (Beiersdorfer & Wargelin 1994), which demonstrated the possibility of measuring the Fe xvii spectrum from an EBIT source. This spectroscopic capability was recently used to test the predictions of the Fe xxiv line emission from different astrophysical spectral modeling codes (Savin et al. 1996).

The spectrometer used in this experiment is a flat crystal spectrometer described by Beiersdorfer & Wargelin (1994) and further in Beiersdorfer et al. (1997). Different crystals were employed in the measurements, either cesium acid phthalate (CsAP), thallium acid phthalate (TIAP), potassium acid phthalate (KAP), or rubidium acid phthalate (RAP) crystals with  $2d$  spacing of 25.68, 25.76, 26.58, and 26.12 Å, respectively (Burek 1976). The region of the electron beam in which the interaction between the ions and the beam occurs is about 2 cm long and 60  $\mu\text{m}$  wide (Levine et al. 1989); therefore, the beam acts as a line source for the spectrometer and no slit assembly is required. Because the region being observed is in the soft X-ray range, the spectrometer must operate in vacuum to avoid absorption of the X-rays by air. To separate the vacuum in EBIT ( $\sim 10^{-10}$  torr) from the spectrometer ( $\sim 10^{-5}$  torr), a polyimide foil that is 1  $\mu\text{m}$  thick and 25 mm in diameter is placed between the spectrometer and EBIT.

The detector used in this experiment is a single-wire, one-dimensional proportional counter with a  $0.8 \times 8.0 \text{ cm}^2$  window (Borkowski & Kopp 1968). The window is covered with a 4  $\mu\text{m}$  polypropylene foil coated with a few hundred angstroms of aluminum. There is a continuous flow of P-10 gas (10% methane and 90% argon) through the detector at a constant pressure of about 1 atm. The polypropylene foil in conjunction with the 1  $\mu\text{m}$  polyimide foil separating the spectrometer from EBIT allows greater than 5% transmission of X-rays whose wavelength is less than 19 Å (Markert 1991), which are detected with near 100% quantum efficiency (Beiersdorfer & Wargelin 1994). The resolving power of the spectrometer in this experiment is limited by the crystals and is  $\lambda/\Delta\lambda \sim 500\text{--}700$  in first order and  $\lambda/\Delta\lambda \sim 1300\text{--}1500$  in second order.

## 3. SPECTRAL MEASUREMENTS AND LINE IDENTIFICATION

The angle that the crystal makes with the incident radiation from EBIT determines the wavelength that is reflected according to Bragg's law:

$$n\lambda = 2d \sin \theta, \quad (1)$$

where  $n$  is the order of the reflection,  $\lambda$  is the wavelength reflected,  $d$  is the crystal lattice spacing, and  $\theta$  is the Bragg angle. The wavelength interval observable at a given setting of the spectrometer is between 1 and 2 Å. To cover the wavelength range from 9.8 to 17.5 Å, a total of 12 mutually overlapping spectra were recorded. Each spectrum was taken at a beam energy of either  $1230 \pm 30$  or  $1150 \pm 30 \text{ eV}$  and at a beam current of  $40 \pm 5 \text{ mA}$ , which corresponds to an electron density of  $\sim 10^{12} \text{ cm}^{-3}$ . The ionization potential of Fe xvi is 490 eV and that of Fe xvii is 1262 eV (Cowan 1981); so, setting the beam to an energy of either

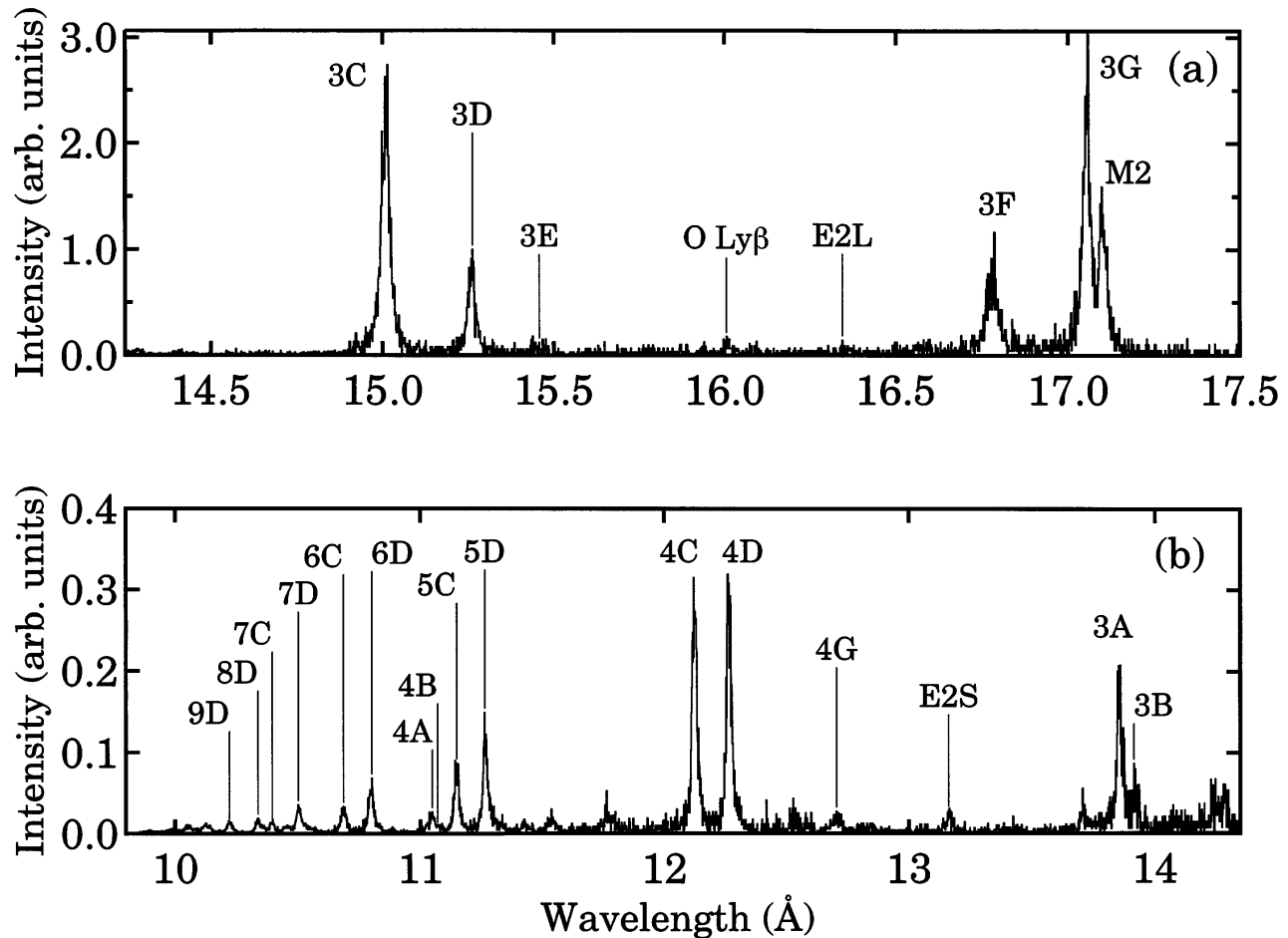


FIG. 1.—Overview of the nine mutually overlapping spectra of the L-shell emission of Fe xvii: (a) 14.25–17.6 Å, (b) 9.8–14.33 Å

1230 or 1150 eV produces Fe xvii ions almost exclusively. The integration time for a single spectrum varied from 30 minutes to 6 hr depending on the count rate in the lines being observed.

An overview of the spectral range studied in this experiment is shown in Figure 1. This spectrum is a concatenation of the nine spectra acquired in first-order Bragg reflection at different overlapping crystal settings. The connections of the separate spectra take place at 10.27, 10.59, 11.58, 12.63, 13.77, 15.09, 15.89, and 16.68 Å. Spectra below 11.58 Å were taken with a TIAP crystal, while the spectra above 11.58 Å were taken with a CsAP crystal. The relative efficiency of the spectrometer and the different crystals, as discussed below, were taken into account in producing the spectra shown in Figure 1 and 2. It should be noted that the scale in Figure 1b is about 1/10 that of Figure 1a.

Because the resolving power diminishes as the wavelength decreases, a second set of measurements was made covering the low-wavelength region from 9.8 to 10.8 Å, which contains the high- $n$  L-shell transitions up to the ionization limit. These measurements were performed in second-order Bragg reflection, providing higher resolving power. The resulting spectrum is shown in Figure 2, which is a concatenation of three crystal settings connected at 10.17 and 10.42 Å. The second-order spectra were taken with the TIAP crystal. The spectrometer response is also folded into the second-order spectrum. This spectrum is normalized to the first-order spectrum by matching the

counts in the line labeled 7D taken both in first and second order.

A listing of the observed transitions is given in Table 1. The Fe xvii transitions were identified by comparison with previous measurements (Parkinson 1973, 1975; Hutcheon et al. 1976; McKenzie et al. 1980; Phillips et al. 1982; McKenzie & Landecker 1982; McKenzie et al. 1985) and by comparing the observation with our calculated intensities and wavelengths. We identify lines of the type  $2p^5nd_{3/2} \rightarrow 1P_1 \rightarrow 2p^6 \rightarrow 1S_0$  (labeled  $nC$ ) up to  $n = 10$ , and  $2p^5nd_{5/2} \rightarrow 3D_1 \rightarrow 2p^6 \rightarrow 1S_0$  up to  $n = 11$ ; however, lines of the type  $np \rightarrow 2s$  (labeled  $nA$  and  $nB$ ) are identified only up to  $n = 5$ . For  $n \geq 6$ , the energy levels for this type of transition lie above the ionization energy for the neon-like ion. As a result, the  $nA$  and  $nB$  transitions for  $n \geq 6$  preferentially autoionize and are not observed. The labeling scheme used here follows that of Parkinson (1973) with the exception of M2, which Parkinson labels 3H, and the electric quadrupole lines E2L and E2S, which Parkinson does not identify.

The electric quadrupole lines observed here are the first to be identified in the Fe xvii L-shell spectrum. Following the earlier notation, the lines at 16.350 and 13.153 Å are labeled E2S and E2L in Figure 1. There are two other E2 lines that have been seen in spectral measurements of higher  $Z$  neon-like ions (Dietrich et al. 1985; Beiersdorfer et al. 1986; Beiersdorfer et al. 1988). These had been labeled E2M (“middle”) and E2U (“upper”). In Fe xvii, our calculations predict the wavelength of the E2M line as 16.257 Å and its

TABLE 1  
SUMMARY OF MEASURED WAVELENGTHS OF Fe XVII

$\lambda$ (Å)								
LABEL	TRANSITION	Present Measurement	Phillips et al. 1982	McKenzie et al. 1980	Boiko et al. 1978	Mewe et al. 1985	HULLAC	
M2	$2p^6\ ^1S_0-1s^22s^22p_{1/2}^2\ 2p_{3/2}^3\ 3s_{1/2}\ ^3P_2$	17.096(1)	17.096	17.084	...	17.100	17.118	17.118
3G	$2p^6\ ^1S_0-1s^22s^22p_{1/2}^2\ 2p_{3/2}^3\ 3s_{1/2}\ ^3P_1$	17.051(1)	17.051	17.043	...	17.054	17.071	17.071
3F	$2p^6\ ^1S_0-1s^22s^22p_{1/2}^2\ 2p_{3/2}^4\ 3s_{1/2}\ ^1P_1$	16.780(2)	16.775	16.775	...	16.787	16.795	16.795
E2L	$2p^6\ ^1S_0-1s^22s^22p_{1/2}^2\ 2p_{3/2}^3\ 3p_{1/2}\ ^3D_2$	16.350(8)	...	...	...	...	16.351	16.351
3E	$2p^6\ ^1S_0-1s^22s^22p_{1/2}^2\ 2p_{3/2}^3\ 3d_{3/2}\ ^3P_1$	15.453(5)	15.451	15.456	15.449	15.458	15.470	15.470
3D	$2p^6\ ^1S_0-1s^22s^22p_{1/2}^2\ 2p_{3/2}^3\ 3d_{3/2}\ ^3D_1$	15.261(2)	15.255	15.262	15.260	15.262	15.272	15.272
3C	$2p^6\ ^1S_0-1s^22s^22p_{1/2}^2\ 2p_{3/2}^3\ 3d_{3/2}\ ^1P_1$	15.014(1)	15.012	15.013	15.013	15.013	15.014	15.014
3B	$2p^6\ ^1S_0-1s^22s_{1/2}^2\ 2p_{3/2}^6\ 3p_{1/2}\ ^3P_1$	13.892(3)	13.890	...	13.892	13.890	13.840	13.840
3A	$2p^6\ ^1S_0-1s^22s_{1/2}^2\ 2p_{3/2}^6\ 3p_{3/2}\ ^1P_1$	13.825(2)	13.824	13.847	13.834	13.824	13.793	13.793
E2S	$2p^6\ ^1S_0-1s^22s_{1/2}^2\ 2p_{3/2}^6\ 3d_{3/2}\ ^1D_2$	13.153(4)	...	...	...	...	13.131	13.131
4G	$2p^6\ ^1S_0-1s^22s^22p_{1/2}^2\ 2p_{3/2}^3\ 4s_{1/2}\ ^3P_1$	12.695(9)	12.681	...	12.678	12.681	12.700	12.700
4D	$2p^6\ ^1S_0-1s^22s^22p_{1/2}^2\ 2p_{3/2}^3\ 4d_{5/2}\ ^3D_1$	12.266(1)	12.263	12.276 <sup>a</sup>	12.269	12.263	12.275	12.275
4C	$2p^6\ ^1S_0-1s^22s^22p_{1/2}^2\ 2p_{3/2}^4\ 4d_{3/2}\ ^1P_1$	12.124(1)	12.122	12.127 <sup>a</sup>	12.125	12.122	12.135	12.135
5D	$2p^6\ ^1S_0-1s^22s^22p_{1/2}^2\ 2p_{3/2}^3\ 5d_{5/2}\ ^3D_1$	11.254(2)	11.250	11.255 <sup>a</sup>	11.249	11.255	11.262	11.262
5C	$2p^6\ ^1S_0-1s^22s^22p_{1/2}^2\ 2p_{3/2}^4\ 5d_{3/2}\ ^1P_1$	11.131(2)	11.129	11.140	11.132	11.140	11.142	11.142
4B	$2p^6\ ^1S_0-1s^22s_{1/2}^2\ 2p_{3/2}^6\ 4p_{1/2}\ ^3P_1$	11.051(5)	...	...	...	11.034	11.030	11.030
4A	$2p^6\ ^1S_0-1s^22s_{1/2}^2\ 2p_{3/2}^6\ 4p_{3/2}\ ^1P_1$	11.026(3)	...	...	...	...	11.012	11.012
6D	$2p^6\ ^1S_0-1s^22s^22p_{1/2}^2\ 2p_{3/2}^3\ 6d_{5/2}\ ^3D_1$	10.770(2)	10.768	10.778 <sup>a</sup>	10.774	10.778	10.781	10.781
6C	$2p^6\ ^1S_0-1s^22s^22p_{1/2}^2\ 2p_{3/2}^4\ 6d_{3/2}\ ^1P_1$	10.657(2)	10.654	...	10.640	10.665	10.668	10.668
7D	$2p^6\ ^1S_0-1s^22s^22p_{1/2}^2\ 2p_{3/2}^3\ 7d_{5/2}\ ^3D_1$	10.504(2)	...	...	10.506	...	10.511	10.511
7C	$2p^6\ ^1S_0-1s^22s^22p_{1/2}^2\ 2p_{3/2}^4\ 7d_{3/2}\ ^1P_1$	10.393(2)	...	10.382	10.386	10.382	10.403	10.403
8D	$2p^6\ ^1S_0-1s^22s^22p_{1/2}^2\ 2p_{3/2}^3\ 8d_{5/2}\ ^3D_1$	10.333(3)	...	...	...	...	10.345	10.345
8C	$2p^6\ ^1S_0-1s^22s^22p_{1/2}^2\ 2p_{3/2}^4\ 8d_{3/2}\ ^1P_1$	10.229(4)	...	...	...	...	10.239	10.239
9D	$2p^6\ ^1S_0-1s^22s^22p_{1/2}^2\ 2p_{3/2}^3\ 9d_{5/2}\ ^3D_1$	10.221(4)	...	...	...	...	10.232	10.232
10D	$2p^6\ ^1S_0-1s^22s^22p_{1/2}^2\ 2p_{3/2}^3\ 10d_{5/2}\ ^3D_1$	10.142(6)	...	...	...	...	10.155	10.155
9C	$2p^6\ ^1S_0-1s^22s^22p_{1/2}^2\ 2p_{3/2}^4\ 9d_{3/2}\ ^1P_1$	10.121(6) <sup>b</sup>	...	...	...	...	10.128	10.128
5A	$2p^6\ ^1S_0-1s^22s_{1/2}^2\ 2p_{3/2}^6\ 5p_{3/2}\ ^1P_1$	10.121(6) <sup>b</sup>	...	10.136 <sup>a</sup>	...	10.136	10.114	10.114
11D	$2p^6\ ^1S_0-1s^22s^22p_{1/2}^2\ 2p_{3/2}^3\ 11d_{5/2}\ ^3D_1$	10.088(6)	...	...	...	...	10.097	10.097
10C	$2p^6\ ^1S_0-1s^22s^22p_{1/2}^2\ 2p_{3/2}^4\ 10d_{3/2}\ ^1P_1$	10.046(5)	...	...	...	...	10.051	10.051

<sup>a</sup> Blend with other charge states of iron or ion of another element.

<sup>b</sup> This is the value for the 5A-9C blend (see Fig. 2).

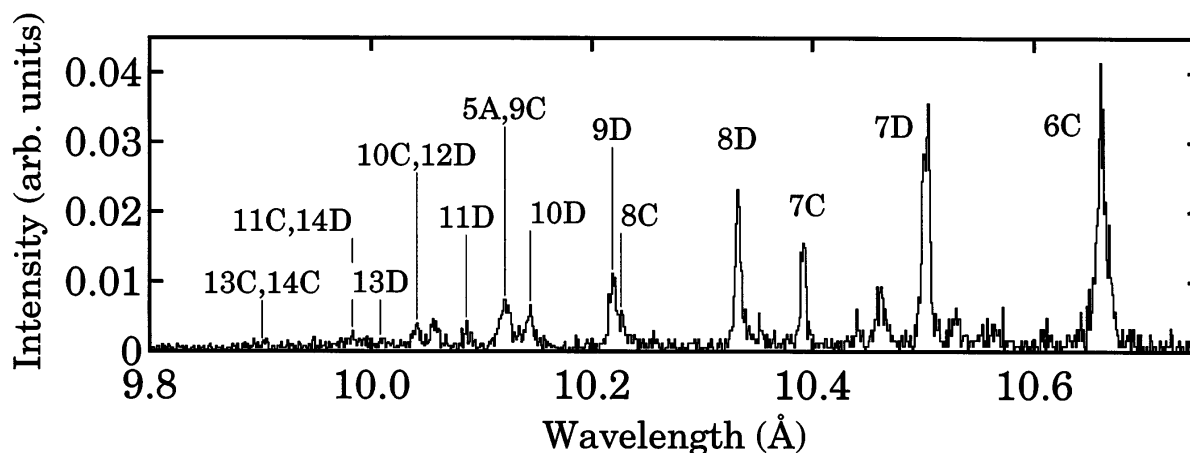


FIG. 2.—Higher  $n \rightarrow 2$  emission taken in second order. This is a concatenation of three spectra connected at 10.17 and 10.42 Å. The unmarked lines are Fe xviii emission, emission from residual calibration gases, or contaminants indigenous to EBIT.

intensity to be about two-thirds the size of E2L; the wavelength of E2U is predicted to be 16.004 Å with an intensity of about the same size as E2L. Neither of these lines are identified in our spectrum. E2U is not identified owing to a coincidence with the O viii Ly $\beta$  transition and possibly an Fe xviii transition, which are situated at 16.006 and 16.009 Å, respectively. E2M is not identified because it is too weak relative to the background level.

Several lines are seen in Figures 1 and 2 that are not marked or identified in Table 1. There are three sources for these lines: background ions indigenous to the trap region at EBIT, lines produced by residual gases left over from calibration spectra, and contributions from Fe xviii line emission. Fe xviii is present even though the nominal beam energy is at a value below the ionization potential of Fe xvii because of the finite spread in the energy distribution of the beam electrons. This distribution is Gaussian with a width of about 30–50 eV (Levine et al. 1989; Beiersdorfer et al. 1992). Assuming a 30 eV width, less than 1% of the beam electrons in an 1150 eV beam have an energy that lies above the ionization energy for Fe xvii ( $E_{\text{ion}} = 1262$  eV; Cowan 1981) and may create Fe xviii ions, while approximately 8% of the beam lies above the ionization potential for a 1230 eV beam with a 30 eV width. Although only a small fraction of Fe xviii is produced (we estimate 4% for the 1150 eV beam and 10% for the 1230 eV beam), it is possible to excite and observe the strongest Fe xviii lines in the spectrum. These then have an intensity comparable to the weakest Fe xvii lines observed. For example, the strongest Fe xviii line at 14.18 Å is comparable in intensity to most high- $n$  transition Fe xvii lines as well as line 3B. The production of Fe xviii ions can be prevented by selecting a lower beam energy. Unfortunately, it was necessary to raise the beam energy in the lower wavelength region in order to ensure the excitation of the Fe xvii high- $n$  transitions, which have excitation energies very close to the ionization limit. Fe xviii emission is easily identified by comparing spectra taken at beam energies well above and well below the ionization potential for Fe xvii. The Fe xviii lines in the first-order spectrum (Fig. 1) identified this way are at 16.09, 15.63, 14.18, and 11.50 Å. Similarly, lines from Fe xviii at 10.53, 10.44, 10.36, and 10.05 Å are seen in the second-order spectrum in Figure 2. By contrast, no significant amount of Fe xvi is present under these measurement conditions.

Gases used for calibration (see § 4) have a tendency to

remain in the trap region for long periods of time and contribute some residual line features to our spectra. These include the O viii Ly $\beta$  at 16.006 Å and the Ne ix  $z$  ( $1s2s\ ^3S_1 \rightarrow 1s^2\ ^1S_0$ ) line at 13.705 Å. We were not able to identify the line at 11.76 Å in the first-order spectrum and at 10.46 Å in the second-order spectrum. It is possible that these correspond to transitions in an intermediate charge state of barium, lanthanum, or tungsten, contaminants that are emitted by the electron gun. As mentioned earlier (see § 2), their presence was minimized by frequently filling and dumping the trap. We have no other indications that any of these elements were present in the trap.

#### 4. WAVELENGTH DETERMINATIONS

Each crystal setting was calibrated separately using well-known lines of helium- or hydrogen-like ions of fluorine, neon, or oxygen. Figure 3 shows a concatenation of the calibration spectra used for the first-order measurement. The lines observed in the calibration spectra include the  $2p \rightarrow 1s$ ,  $3p \rightarrow 1s$ ,  $4p \rightarrow 1s$ , and  $5p \rightarrow 1s$  lines labeled Ly $\alpha$ , Ly $\beta$ , Ly $\gamma$ , and Ly $\delta$ , respectively, in hydrogenic O viii, F ix, and Ne x, and the  $1s2p\ ^1P_1 \rightarrow 1s^2\ ^1S_0$ ,  $1s2p\ ^3P_1 \rightarrow 1s^2\ ^1S_0$ , and  $1s2s\ ^3S_0 \rightarrow 1s^2\ ^1S_0$ , resonance, intercombination, and forbidden lines in helium-like F viii and Ne ix, labeled  $w$ ,  $y$ , and  $z$ , respectively, as well as the  $1s3p\ ^3P_1 \rightarrow 1s^2\ ^1S_0$ ,  $1s4p\ ^3P_1 \rightarrow 1s^2\ ^1S_0$ ,  $1s5p\ ^3P_1 \rightarrow 1s^2\ ^1S_0$ , and  $1s6p\ ^3P_1 \rightarrow 1s^2\ ^1S_0$ , lines in helium-like F viii and Ne ix, labeled K $\beta$ , K $\gamma$ , K $\delta$ , and K $\epsilon$ , respectively. No normalization of the line intensities observed in the individual spectra was attempted, so that some of the line ratios shown are inconsistent with ratios known from other measurements. For example, the K $\gamma$  line in Ne ix is much weaker than normal compared to other K-series line emission because it fell on the edge of the crystal in this particular measurement.

In order to calibrate a given spectral region, the central channel number of each calibration line is found by fitting a Gaussian function to the line profile. This procedure is repeated for all of the calibration lines that fall into a particular wavelength region observed at a given crystal setting. The wavelengths of the helium-like and hydrogenic lines have been calculated with high accuracy, i.e., with an accuracy that exceeds the uncertainty limits of our measurement of the Fe xvii lines (Garcia & Mack 1965; Drake 1988; Vainstein & Safranovskaya 1985); therefore, a corresponding Bragg angle can be found via Bragg's law (eq. [1]). Once the

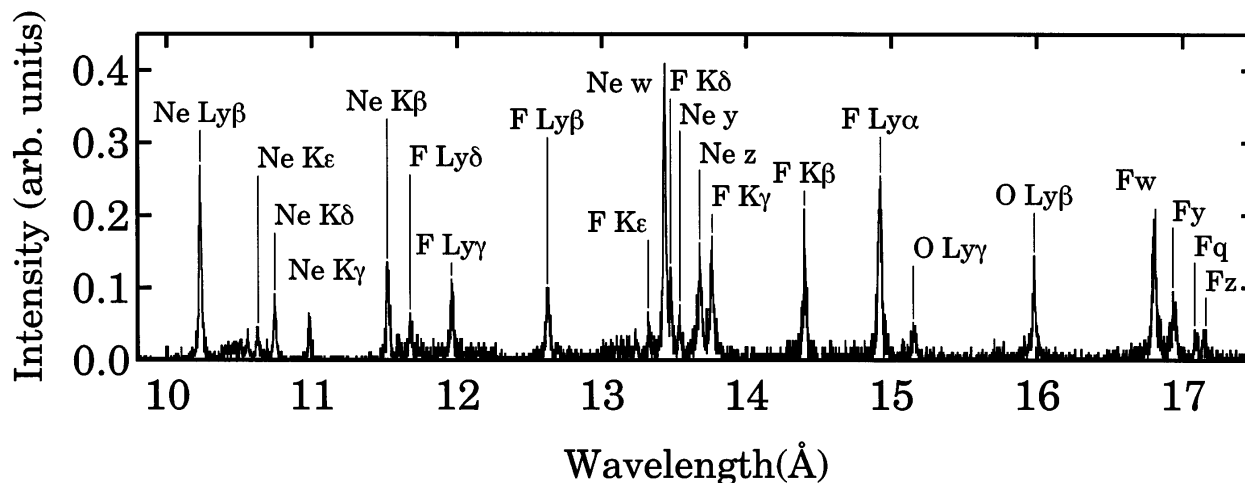


FIG. 3.—Calibration lines. The spectrum shown is a composite of several spectra taken under different conditions. The lines are used for wavelength calibration only.

Bragg angle of each calibration line is found, a linear regression from Bragg angle to channel number is conducted. The equation for the line that fits channel number to Bragg angle is then placed into Bragg's Law, giving the following form:

$$n\lambda = 2d \sin(mN_c + b), \quad (2)$$

where  $m$  and  $b$  are the slope and the  $y$ -intercept given by the linear regression of the calibration data, and  $N_c$  is the central channel number of a given line.

The second-order spectra were calibrated with the use of the Ne ix K $\epsilon$ , K $\xi$ , and K $\eta$  and Ne x Ly $\beta$  transitions, as well as with some Fe xvii lines observed in first order. Relying on Fe xvii lines was necessary because only one or two hydrogenic or helium-like calibration lines are present in each spectrum due to the reduced wavelength interval. In particular, the lines in the first region of second order were calibrated with the lines K $\epsilon$ , K $\xi$ , and K $\eta$  of helium-like Ne ix. The second region was calibrated with the Ne x Ly $\beta$  and the first-order measurement of 7C. The third region was calibrated with the Ne x Ly $\beta$ , the first-order measurement of 10C, and the second-order measurement of 9D.

A summary of the measured wavelengths of Fe xvii lines is given in Table 1. The uncertainty in the last digit is given in parentheses after each wavelength. It was determined by the uncertainty in the fit of the centroid of the calibration lines, the uncertainty in the wavelength dispersion, and the uncertainty in the centroid of a given iron line. The positions of several of the high- $n$  transitions are labeled in Figure 2 but are not given wavelength assignments in Table 1. For example, the  $nC$  and  $nD$  transitions for  $n = 12, 13$ , and  $14$  in the second-order spectrum are not given wavelength assignments because they are unresolved or are too weak to be identified with any certainty. Line 11C is not shown in Table 1 because it blends with 14D.

For comparison, we also include in Table 1 solar measurements, other laboratory measurements, and theoretical wavelengths for the same transitions. Approximately half of the lines identified in EBIT and solar measurements agree within the respective wavelength uncertainty. Solar measurements presented by Phillips et al. (1982) consistently assign wavelengths that are below our measurements, while solar measurements by McKenzie et al. (1980) are generally

higher. A comparison with measurements obtained from a high-density vacuum spark device by Boiko et al. (1978) shows that the wavelengths of 50% of lines we both identify do not agree, although it should be noted that the discrepancies are neither consistently higher nor lower. The assignments from the vacuum spark data have inherently lower accuracy than our measurements due to blending with emission from other charge states of iron, dielectronic satellites, and ions of other elements.

The seventh column of Table 1 contains wavelengths tabulated by Mewe, Gronenschild, & van den Oord (1985) for use in the spectral fitting code MEKA. These are tabulated from compilations of measured values such as those given in Doschek & Cowan (1984). Of the 17 transitions tabulated by Mewe et al. (1985), only six agree within our error bars. It should be further noted that we identify a total of 28 transitions, while Mewe et al. (1985) only incorporate 17. One transition that Mewe et al. (1985) include, which is not included in our identification, is  $4F(2p^5 4s_{1/2} \ ^1P_1 \rightarrow 2p^6 \ ^1S_0)$ . It is not included in our wavelength identification because it is too weak to be identified in our measurements and is thus not an important feature of the Fe xvii L-shell spectrum under our experimental conditions.

The MEKA code has recently been updated using new Fe xvii atomic data generated with HULLAC (Hebrew University/Lawrence Livermore Atomic Code) atomic physics package (see Liedahl, Osterheld, & Goldstein 1995). In the last column of Table 1 are the wavelengths calculated by HULLAC. HULLAC is used to calculate line positions according to the relativistic multiconfigurational parametric potential method (Klapisch 1971). By comparing the values calculated by HULLAC to those measured at EBIT, clear and systematic differences are found. The measured wavelengths of all transitions of the type  $nl \rightarrow 2p$  are significantly shorter than the calculated values, while those transitions of the type  $nl \rightarrow 2s$  are significantly longer than the calculated values. For the values presented here, the differences are between  $+10$  and  $+20$  mÅ for transitions that terminate in a  $2p_{1/2}$  or  $2p_{3/2}$  vacancy and approximately  $-30$  mÅ for transitions that terminate in a  $2s_{1/2}$  vacancy. This systematic behavior has been observed and documented in measurements of other neon-like ions by Beiersdorfer et al. (1986, 1988). The present measurement

demonstrates that systematic shifts also affect lines calculated in the Fe XVII ion.

### 5. LINE INTENSITIES

In order to make a reliable comparison of the intensities of the various Fe XVII lines, we need to account for the spectral response function of the spectrometer and normalize the spectra obtained from different crystal settings to each other. The response curve of the spectrometer, which includes both the foil and the crystal response, was calculated as a function of wavelength. The dominant source of absorption is caused by the polyimide and the polypropylene foils whose foil transmission varies smoothly from 55% at 10 Å to 5% at 18 Å. The variation in the crystal response for CsAP and TIAP was predicted by G. Hölzer, O. Wehrhan, and E. Förster (1997, private communication). It varies by a factor of about 3 for TIAP and 1.5 for CsAP. By comparison, the response of the detector itself was nearly constant.

We calibrated the response function of the spectrometer using an X-ray tube. Employing either an aluminum or a copper target, bremsstrahlung X-radiation was created to illuminate the spectrometer for crystal settings from a Bragg angle of 18°–45°. The measured response agree with those of the calculations within the accuracy of the measurement (about 12%). The response adjustment is estimated to be accurate to within a few percent for lines that are less than 0.3 Å apart and approximately 8% over the entire wavelength range.

Knowing the spectrometer response curve for each crystal, the 12 spectra measured were normalized in the following way to produce the spectra shown in Figures 1 and 2. Each spectrum above 11.58 Å was normalized to  $\lambda 15.01$  by matching the integrated intensity of the overlapping regions in adjoining spectra. After this normalization, the spectrometer response curve employing the CsAP crystal was folded into the spectra. The region taken with TIAP was normalized to 5D, i.e., the transition  $2p^5 5d_{5/2} \ ^3D_1 \rightarrow 2p^6 \ ^1S_0$ , after which the response for the TIAP was folded into the spectrum. Once both TIAP and the CsAP spectra had been separately normalized and their respective response curves had been accounted for, they were joined by matching the integrated intensity of overlapping regions taken with both TIAP and CsAP crystals.

The CsAP and TIAP crystals have M- and N-shell absorption edges, respectively, in the spectral range of interest. These lie at 14.65 and 17.22 Å for TIAP and at 16.75 and 17.07 Å for CsAP (Henke, Gullikson, & Davis 1993). Near such edges, the crystal response is no longer a slowly varying function of wavelength and is thus not as well defined. For the particular measurement of the relative intensities of the  $\lambda 15.01$  and  $\lambda 15.26$  lines, we avoided these absorption edges by employing RAP and KAP crystals. These crystals have no absorption edges in this wavelength region (Henke et al. 1993), and no special consideration for absorption features needed to be made. The response used for evaluating the relative intensities of the lines  $\lambda 15.01$  and  $\lambda 15.26$  is based on integrated crystal reflectivities derived from Henke et al. (1993) and our own foil transmission calculation. The response adjustment reduces the ratio by approximately 10% and is the same for both crystals.

The response curve of the spectrometer not only depends on the energy of the incident radiation but also on the polarization of the radiation. This is a result of the fact that

crystals act as polarimeters and thus reflect the two components of linearly polarized radiation differently (Burek 1976; Beiersdorfer et al. 1996). Lines generated at EBIT are linearly polarized because of the directionality of the electron beam, and this effect must be accounted for when considering line intensities (Beiersdorfer et al. 1996). No such considerations were taken into account in Figures 1 and 2. However, at the beam energies used in this experiment, transitions of the type the  $nd \rightarrow 2p$  are populated predominantly by direct electron-impact excitation and have virtually the same amount of polarization,  $P = +0.40$  (K. Reed 1997, private communication). Thus, polarization-dependent effects cancel when taking intensity ratios involving these transitions. In contrast, ratios involving  $ns \rightarrow 2p$  or  $np \rightarrow 2s$  transitions are produced in large part by radiative cascades (Smith et al. 1985; Louergue & Nussbaumer 1973), and therefore, the value of the polarization of each of these transitions cannot be calculated by considering only the excitation cross sections of magnetic sublevels from the ground level but must include detailed radiative processes from all feeder levels, which is beyond the present analysis. In the following, we therefore concentrate only on ratios involving the  $nC$  and  $nD$  transitions.

#### 5.1. The $nd_{5/2} \rightarrow 2p^6$ and $nd_{3/2} \rightarrow 2p^6$ Line Intensities

Plots of the intensity ratios of  $nD$  to 5D,  $nC$  to 5C, and  $nC$  to  $nD$  are shown in Figures 4, 5, and 6, respectively. The uncertainty limits plotted for each ratio in Figures 4 and 5 reflect the uncertainty in the spectrometer response curve, the normalization of adjoining spectra, and the statistical uncertainty from the counts in each line. Figure 6, on the other hand, gives ratios of transitions taken from the same spectrum, removing the uncertainty due to the normalization from spectrum to spectrum as well as reducing the uncertainty caused by the crystal response. It should also be noted, with regard to Figure 6, that the value of the ratio of  $\lambda 15.01$  to  $\lambda 15.26$  represents the average value measured with RAP and KAP crystals. Any uncertainty due to blending of Fe XVII with lines of Fe XVIII is ruled out by comparing spectra taken at beam energies above threshold for Fe XVII and thus identifying any Fe XVIII lines that may contaminate the Fe XVII spectrum (see § 3). Of the Fe XVIII lines seen

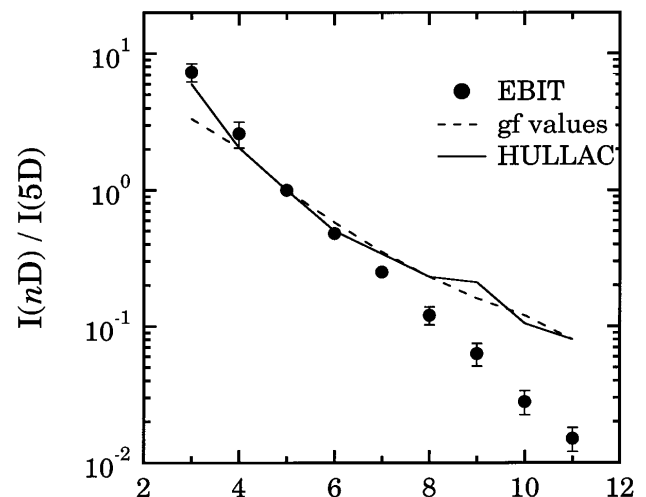


FIG. 4.—Measured intensity ratios of the transitions  $2p^5 nd_{5/2} \ ^3D_1 \rightarrow 2p^6 \ ^1S_0$  (labeled  $nD$ ) to  $2p^5 5d_{5/2} \ ^3D_1 \rightarrow 2p^6 \ ^1S_0$  (labeled 5D) compared to  $gf$ -values and ratios calculated with HULLAC.

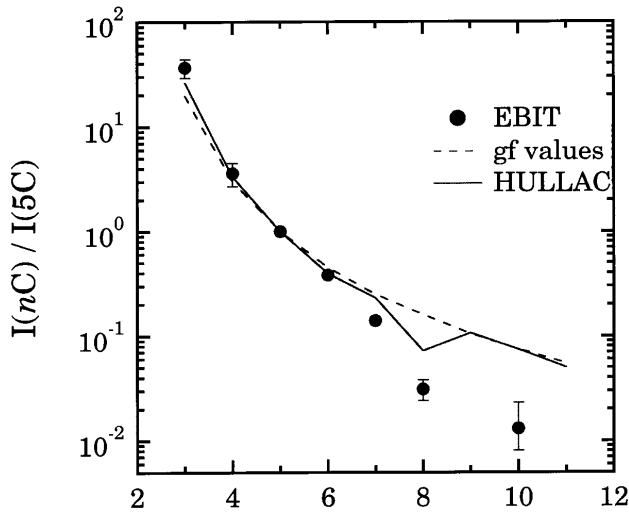


FIG. 5.—Measured intensity ratios of the transitions  $2p^5nd_{3/2} \ ^1P_1 \rightarrow 2p^6 \ ^1S_0$  (labeled  $nC$ ) to  $2p^55d_{3/2} \ ^1P_1 \rightarrow 2p^6 \ ^1S_0$  (labeled  $5C$ ) to  $gf$ -values and ratios calculated with HULLAC.

in the Fe xvii spectrum, none are coincident with the  $nC$  or  $nD$  transitions. Similarly, background contributions can be ruled out by taking spectra in the same wavelength region while no iron is injected into the trap. No coincident background lines were observed.

Ratios of Fe xvii  $nC$  and  $nD$  line emission that have been left out of these plots involve unresolved lines (Fig. 1 and 2). It should be noted that although 10C is shown in Figure 2 as blending with 12D, it is still included in Figures 5 and 6. To permit this, we estimated the intensity of 12D by extrapolating its value from Figure 4 and then appropriately subtracting its effect from the intensity ratios involving 10C, i.e., 10C/5C and 10C/10D. The extrapolation shows that 12D is weak compared to 10C so that this correction is relatively minor. In fact, in Figure 5, the upper limit of 10C/5C is given by the noncorrected value of 10C/5C, i.e., the value with the 12D contamination. Similarly, in Figure

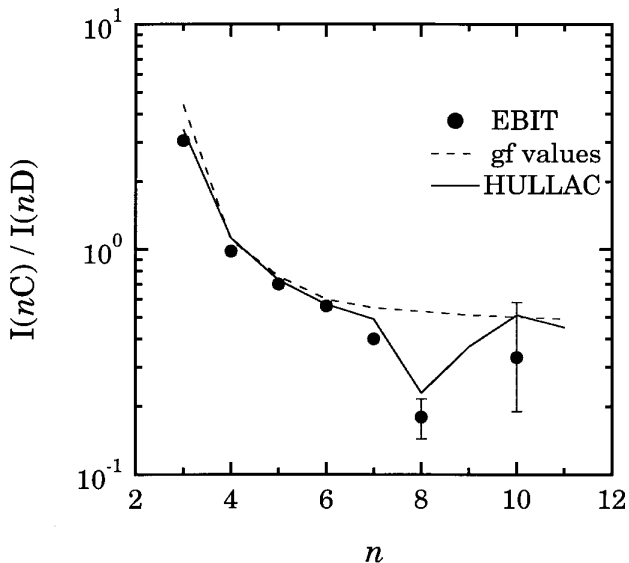


FIG. 6.—Measured intensity ratios of the transitions  $2p^5nd_{3/2} \ ^1P_1 \rightarrow 2p^6 \ ^1S_0$  to  $2p^5nd_{5/2} \ ^3D_1 \rightarrow 2p^6 \ ^1S_0$  (i.e.,  $I_{nC}/I_{nD}$ ) to  $gf$ -values and ratios calculated with HULLAC.

6, the upper limit for the error bar on 10C/10D is shown as the value of 10C/10D with the 12D contamination.

In Figures 4, 5, and 6, we compare our measured intensity ratios to those predicted by HULLAC and  $gf$ -values. HULLAC calculates distorted wave cross sections using the quasi-relativistic distorted wave method on a grid of electron energies rather than at single electron energies (Bar-Shalom et al. 1988), while the  $gf$ -values are calculated using a multiconfigurational Dirac Fock code based on pure transition rates. By comparing the relative intensity of transitions  $nD$  to  $5D$  where  $3 \leq n \leq 11$ , we show in Figure 4 that both theoretical sets of ratios overestimate the ratios for high  $n$  and underestimate the ratios for low  $n$ , although HULLAC displays better agreement with  $n = 3$ . Similarly, in Figure 5 we show the relative intensities of the  $nC$  to  $5C$  transitions. For  $n = 4, 5$ , and  $6$ , there is excellent agreement with the HULLAC model and good agreement with the  $gf$ -values. Again, we find that both sets of calculated values decrease more slowly with  $n$  than the measured values.

For reasons stated earlier, measured ratios of the type  $I(nC)/I(nD)$ , plotted in Figure 6, are the most reliable. Both HULLAC and the  $gf$ -values seem to follow the data very closely, with the exception of  $n = 8$ , where both the measured values and HULLAC show a large dip. This dip is caused by configuration interaction between states with nearly degenerate energy levels. In particular, the upper levels of lines 8C and 9D are nearly degenerate and therefore interact strongly. The effect of such degeneracies on intensity ratios has been observed before from similar transitions in Mo xxxiii (Rice et al. 1995). The  $gf$ -values do not reproduce the dip because the calculations only include configuration interaction between levels of the same principal quantum number ( $n = 8$  in this case). The presence of this dip in both the measurement and in HULLAC demonstrates the necessity of including configuration interaction among levels of different principal quantum number in theoretical models in order to provide accurate modeling of spectra. We point out that the total amount of flux contained in all of the transitions  $nC$  and  $nD$  where  $n \geq 5$  and  $nA$  and  $nB$  transitions with  $n \geq 4$  relative to the line  $\lambda 15.01$  is  $0.13^{+0.04}_{-0.03}$ . This is a significant fraction of the Fe xvii L-shell emission, and it is missing from thermal emission codes (Liedahl & Brickhouse 1998). It must be included in spectral emission models in order to accurately predict emission in the 9.8–11.2 Å region; if not included, the Fe xvii flux will be substantially underestimated in this wavelength range.

## 5.2. Intensity Ratio of the $\lambda 15.01$ and $\lambda 15.26$ Lines

A substantial difference has been noted between the calculated value for the intensity ratio of the lines  $\lambda 15.01$  and  $\lambda 15.26$  and those measured in solar spectra. A definitive comparison between calculation and solar values, however, is impossible because of the large scatter among the theoretical results. This is illustrated in Table 2, which lists the ratios of collision strengths, rate coefficients, and cross sections from calculations and intensity ratios from solar measurements. In order to make a definitive comparison as well as to correctly identify physical processes that may occur in the Sun, this ratio has been measured at EBIT. The results for different energies are given in Table 2.

Although our measurements were made with a monoenergetic electron beam, while the theoretical data consist of cross sections (Hagelstein & Jung 1987), collision



TABLE 2  
LINE RATIOS OF THE INTENSITY OF THE TRANSITION 3C TO 3D

Source	Electron Energy	Ratio [ $I(\lambda 15.01)/I(\lambda 15.26)$ ]
Theory <sup>a</sup> :		
Mann 1983 .....	1030 eV	2.92
Bely & Bely 1967 .....	826 eV	3.11
Smith et al. 1985 .....	862 eV (temperature)	3.29
HULLAC .....	1265 eV	3.40
Zhang et al. 1987 .....	980 eV	3.78
Waljeski et al. 1994 .....	216 eV (temperature)	3.80
Hagelstein & Jung 1987 .....	1100 eV	3.92
Mohan et al. 1997 .....	1245 eV	3.99
Bhatia & Doschek 1992 .....	1245 eV	4.28
Cornille et al. 1994 .....	1156 eV	4.57
Bhatia et al. 1985 .....	952 eV	4.74
Solar <sup>b</sup> :		
Blake et al. 1965 .....	Nonflaring active region	$1.60 \pm 0.32$
Waljeski et al. 1994 .....	Nonflaring active region	$1.87 \pm 0.21$
Parkinson 1975 .....	Nonflaring active region	$2.05 \pm 0.1$
Hutcheon et al. 1976 .....	Flaring active region	$2.59 \pm 0.1$
McKenzie et al. 1980 .....	Flaring active region	$2.75 \pm 0.7$
EBIT <sup>c</sup> :		
RAP .....	$1150 \pm 30$ eV	$2.93 \pm 0.16$
KAP .....	$1150 \pm 30$ eV	$3.15 \pm 0.17$
	$850 \pm 30$ eV	$2.77 \pm 0.19$
	$1300 \pm 30$ eV	$3.00 \pm 0.20$

NOTE.—Results are compared with calculated values and measured values from the Sun.

<sup>a</sup> Theoretical ratios of unitless collision strengths ( $\Omega_{ij}$ ) with the exception of Waljeski et al. 1994, who report an emissivity; Smith et al. 1985, who report a rate coefficient; and Hagelstein & Jung 1987 and HULLAC, who both give cross sections.

<sup>b</sup> Measured solar values from either a flaring or a nonflaring active region.

<sup>c</sup> EBIT values at various beam energies employing either KAP or RAP crystal.

strengths (Bely & Bely 1967; Mann 1983; Bhatia, Feldman, & Seely 1985; Zhang et al. 1987; Bhatia & Doschek 1992; Mohan, Sharma, & Eissnar 1997), and excitation rate coefficients (Smith et al. 1985), they are all equivalent when considering the intensity ratio of  $\lambda 15.01$  and  $\lambda 15.26$ , and it is valid to compare all values with each other. Moreover, it is also valid to compare our measurements to those measured from the Sun, although those results are from a plasma with a presumably Maxwellian electron distribution. The validity of these comparisons is shown in the following.

The measured values from EBIT are ratios of photon flux corrected by the response function of the spectrometer. In the low-density or coronal limit as produced at EBIT, where collisional deexcitation of upper levels is unimportant, the measured value is given by

$$I_{ji} = \eta(\lambda_{ji}) \beta_{ji} v \sigma_{ij} \cdot n_e n_{\text{FeXVII}}, \quad (3)$$

where  $j$  and  $i$  denote the initial (upper) and final (lower) level of the transition,  $\eta(\lambda_{ji})$  is the response function of the spectrometer as a function of wavelength,  $\beta_{ji}$  is the branch-

ing ratio,  $v$  is the electron velocity,  $\sigma_{ij}$  is the effective total cross section for electron-impact excitation,  $n_e$  is the electron density, and  $n_{\text{FeXVII}}$  is the density of Fe xvii ions. The measured ratios are, therefore, the ratio of the measured intensities (eq. [3]) after the response function has been divided out. In the case in which both transitions share the same lower level, the ratio is given by

$$\frac{I_{ji}}{I_{ki}} = \frac{\beta_{ji} v \sigma_{ij} \cdot n_e n_{\text{FeXVII}}}{\beta_{ki} v \sigma_{ik} \cdot n_e n_{\text{FeXVII}}} = B_{jk} \cdot \frac{\sigma_{ij}}{\sigma_{ik}}, \quad (4)$$

the ratio of the total cross section times the relative branching ratio  $B_{jk} = (\beta_{ji}/\beta_{ki})$ . HULLAC predicts the relative branching ratio between  $\lambda 15.01$  and  $\lambda 15.26$  to be 1.002, which we put to unity, so the quoted ratio in Table 3 given by is

$$\frac{I_{ji}}{I_{ki}} = \frac{\sigma_{ij}}{\sigma_{ik}}, \quad (5)$$

the ratio of the total cross sections.

TABLE 3  
VALUES OF VARIOUS PHYSICAL PARAMETERS INFERRED FROM THE RATIO ( $R$ )  
OF  $I_{\lambda 15.01}/I_{\lambda 15.26}$  FOR THE OPTICALLY THIN CASE MEASURED AT EBIT  
AND COMPARED TO CALCULATIONS BY WALJESKI ET AL. 1994

Parameter	EBIT	Waljeski et al. 1994
$R_{\text{opt.thin}}$ .....	$3.04 \pm 0.12$	3.80
$\tau(R_{\text{Solar}} = 1.90 \pm 0.21)^a$ .....	$2.5^{+0.6}_{-0.9}$	$4.24^{+1.3}_{-1.0}$
$\int n_e dl$ .....	$6.2^{+1.5}_{-2.2} \times 10^{19} \text{ cm}^{-2}$	$1.05 \times 10^{20} \text{ cm}^{-2}$
$n_e$ .....	$3.7^{+2.0}_{-0.7} \times 10^9 \text{ cm}^{-3}$	$2.2^{+0.8}_{-0.4} \times 10^9 \text{ cm}^{-3}$
$dl$ .....	$1.7^{+0.4}_{-0.7} \times 10^{10} \text{ cm}$	$4.7^{+0.9}_{-1.8} \times 10^{10} \text{ cm}$

<sup>a</sup>  $R_{\text{Solar}} = 1.90 \pm 0.21$  is the value for the intensity ratio of  $\lambda 15.01/\lambda 15.26$  measured at the Sun (Waljeski et al. 1994).

The ratios from the theoretical calculations in Table 2 are the collision strength ( $\Omega_{ij}$ ), the total cross section ( $\sigma_{ij}$ ), and the rate coefficients ( $\gamma_{ji}$ ). The collision strength is defined by

$$\Omega_{ij} = \left[ \frac{2m}{\hbar^2} \right] \cdot \omega g_i \sigma_{ij}, \quad (6)$$

where  $\omega$  is the kinetic energy of the impact electron,  $g_i$  is the statistical weight of the ground level,  $\sigma_{ij}$  is the total cross section for the excitation of an electron from the level  $i$  to level  $j$ ,  $m$  is the mass of the electron, and  $\hbar$  is Planck's constant divided by  $2\pi$ . Given that  $g_i = 1$  in the case of interest and that the electron impact energy is the same, the ratios of collision strengths are equal to ratios of the total cross sections.

The rate coefficient may be expressed in terms of the Maxwellian averaged collision strengths by

$$\gamma_{ji} = \frac{8.0 \times 10^{-8} \Omega_{ij}^{\text{eff}}(T)}{g_i (kT)^{1/2}} \exp\left(-\frac{\Delta E}{kT}\right) \text{ cm}^3 \text{ s}^{-1}, \quad (7)$$

where  $kT$  is in electron volts,  $\Delta E$  is the transition energy, and  $\Omega_{ij}^{\text{eff}}(T)$  is the effective collision strength given by

$$\Omega_{ij}^{\text{eff}}(T) = \int_0^\infty \Omega_{ij}\left(\frac{\epsilon}{kT}\right) \exp\left(\frac{-\epsilon}{kT}\right) d\left(\frac{\epsilon}{kT}\right), \quad (8)$$

where  $\epsilon$  is the electron impact energy relative to the transition energy  $\Delta E$ . Therefore, taking the ratio of two rate coefficients evaluated at the same electron temperature leaves a ratio of the effective collision strengths times an exponential factor. The ratio of the exponential factors for the transitions corresponding to  $\lambda 15.01$  and  $\lambda 15.26$  is approximately unity. In order to calculate the effective collision strength for a given transition, the collision strength ( $\Omega_{ij}$ ) is calculated at several different electron impact energies and then a function is fit to the calculated data. This function is then used to evaluate the integral in equation (8). If the collision strength is nearly constant over a wide range of energy, then the effective collision strength and the collision strength are nearly equal. Most calculations show this to be the case as is discussed below. The only rate coefficient quoted in Table 2 is that from Smith et al. (1985), which was calculated at a temperature of  $10^7$  K (862 eV).

The measurements at EBIT were done at single electron beam energies; however, the measurements are applicable to thermal plasmas such as the solar corona because the intensity ratio of  $\lambda 15.01$  and  $\lambda 15.26$  obtained from their respective collision strengths is nearly the same as the relative line intensities calculated for a thermal plasma. The reason is that the dominant excitation process for both lines is electron-impact excitation and that the ratios of collision strengths are nearly constant over a broad band of electron energies. For example, relative collision strengths calculated by Hagelstein & Jung (1987) vary by less than 7% over a range of 2 keV, those calculated by Bhatia & Doschek (1992) vary by less than 5% over an energy band of 2 keV, and those calculated by Cornille et al. (1994) vary by less than 6% over an energy band of 10 keV. Consequently, the difference between the ratio of line intensities calculated by Bhatia & Doschek (1992) and their ratio of collision strengths is approximately 2%, and the difference between the rate coefficients and the collision strengths calculated by Hagelstein & Jung (1987) is less than 2%. Considering the near equality between ratios of collision strengths and rate

coefficients demonstrated by these authors, monoenergetic line ratios from EBIT can be directly compared to those in the Sun, and the ratios observed from each source must be nearly equal unless line formation or scattering processes are present in the Sun that are absent in EBIT. An exception is given by the calculation of Mann (1983), who calculate collision strengths that vary by 23% from 1 to 10 keV. The results from Mann et al. are used by Smith et al. (1985) to calculate their rate coefficients (eq. [7]). Smith et al. find a value of 3.29 for their ratio of rate coefficients, while the ratio of collision strengths found by Mann et al. at an impact energy of 1030 eV is 2.92, a difference of 13%.

To account for the differences between the calculated ratio and those measured in the Sun, several authors have invoked resonance scattering of the flux in  $\lambda 15.01$  (Rugge & McKenzie 1985; Schmelz et al. 1992; Waljeski et al. 1994). Basing the amount of scattering on a comparison of the solar value of  $I(\lambda 15.01)/I(\lambda 15.26)$  with the calculated value, which assumes  $\lambda 15.01$  is optically thin, and noting that the solar ratio is less than the calculated ratio, several authors have inferred physical parameters of the solar corona, such as density (Schmelz et al. 1992; Waljeski et al. 1994), relative iron abundance, and column density along the line of sight (Waljeski et al. 1994). The fact that most solar ratios are also significantly lower than our measurement of the ratio,  $I(\lambda 15.01)/I(\lambda 15.26) = 3.04 \pm 0.12$ , where no scattering occurs, lends support to the possibility of resonance scattering. In order to correctly infer any physical parameter in the solar corona using this ratio a correct optically thin value, i.e., a value at which no resonant scattering occurs, is crucial as the following shows. Using the method described in Waljeski et al. (1994) as well as their emission measure ( $2.3 \times 10^{29} \text{ cm}^{-5}$ ), we infer a column density of  $6.2_{-2.2}^{+1.5} \times 10^{19} \text{ cm}$ , an electron density of  $3.7_{-0.7}^{+2.0} \times 10^9 \text{ cm}^{-3}$ , and an active region path length of  $1.7_{-0.7}^{+0.4} \times 10^{10} \text{ cm}$  from their solar ratio of  $1.90 \pm 0.21$ . Compared to the values given by Waljeski, our column density is a factor of 1.7 lower, making our density a factor of 1.7 higher and our path length nearly a factor of 3 less. Our path length is in much better agreement with the path length derived from Waljeski's broadband image. The calculated ratio given by Waljeski et al. (1994) is 3.8, a difference of about 20% from our value of 3.05. Hence, this 20% difference in the line ratio may cause a factor of nearly 2 difference in density and a factor of 3 difference in path length. These differences are summarized in Table 3.

In addition to adopting the correct optically thin value for this ratio, there are other factors that may contribute to the differences in physical parameters inferred from this ratio. For example, processes such as resonance excitation (Smith et al. 1985; Raymond 1988) or contamination of either line by unresolved Fe xvi lines (Raymond & Smith 1986) may affect this ratio independently of scattering. Once accounted for in EBIT measurements, such processes may eliminate the differences between the EBIT values and those measured in flaring active regions, and therefore, resonant scattering may not be needed to explain these solar measurements. Measurements of the effects of resonant excitation are possible with our source (Beiersdorfer et al. 1990) but are beyond the scope of the present study.

## 6. CONCLUSION

We have presented laboratory measurements of the line emission from the L-shell of Fe xvii in the 9–17.5 Å range

under well-controlled conditions where electron-impact excitation is the dominant excitation process. The transition wavelengths have been measured with an uncertainty of 1–2 mÅ for the stronger lines. Several transitions that have not been observable in the past due to the existence of other charge states of iron, ions of other elements, or low sensitivity have been identified here for the first time including two electric quadrupole transitions, E2S and E2L, as well as many transitions from  $n \geq 5$ . In doing so we have measured lines more reliably than before in the laboratory, nearly doubled the number of lines identified in Fe XVII spectrum, and found systematic offsets in the wavelength tables presently being used to update spectral fitting codes.

Relative intensities of the type  $nd \rightarrow 2p$  have been presented and compared to modeling calculations. It is shown that configuration interaction between levels of different quantum number  $n$  must be included in the theoretical calculations to accurately model the spectrum. The ratio of the total emission from transitions of the type  $nd \rightarrow 2p$ , where  $n \geq 5$ , and the type  $np \rightarrow 2s$ , with  $n = 4$  and 5, in the bandwidth below 11.3 Å relative to the line  $\lambda 15.01$  is  $0.13^{+0.04}_{-0.03}$ . This accounts for all ( $\geq 98\%$ ) of the total flux below 11.4 Å from the iron L-shell emission from Fe XVII resulting from direct-impact excitation followed by radiative cascades.

A value of  $3.04 \pm 0.12$  for the ratio of  $I(\lambda 15.01)/I(\lambda 15.26)$  has been measured at an electron energy of  $1150 \pm 30$  eV. This value is lower than almost all theoretical values but is still somewhat larger than the largest value measured from the Sun. This discrepancy indicates either that processes other than direct-electron excitation followed by radiative cascades play a significant role in the formation of the lines or that resonant scattering affects the intensity of  $\lambda 15.01$  in the Sun. A study of indirect processes that may affect these lines, such as satellites or resonant contributions (Raymond & Smith 1986; Smith et al. 1985; Raymond 1988), as well as

a study of the energy behavior of this ratio must be considered. Although such contributions are predicted to be small at energies above threshold, these processes still need to be measured under controlled laboratory conditions both below the ionization potential for Fe XVI and above the ionization potential for Fe XVII. This is especially important since significant discrepancies were found with the predictions of direct excitation. Measurements of this type are in progress.

The lines involving the transitions of the type  $3s \rightarrow 2p$  and  $3p \rightarrow 2s$  also show strong emission in this bandwidth. These upper levels are populated mostly by cascades (Raymond & Smith 1986; Smith et al. 1985; Loulergue & Nussbaumer 1975), which makes their intensities difficult to calculate accurately. Detailed measurements of the excitation processes and of the polarization of these transitions are also in progress in order to accurately determine their relative intensities.

The combination of all of our measurements presented here—the wavelength identification, the intensity measurement of the high- $n$  transitions, and the measurement of the ratio of  $I(\lambda 15.01)/I(\lambda 15.26)$ —demonstrate that laboratory astrophysics experiments can be used to reliably measure and interpret the iron L-shell emission in the 9.8–17.5 Å band.

We would like to thank M. Chen and K. Reed for their calculations, V. Decaux for his help in acquiring the data, E. Magee and D. Nelson for their technical support, and E. J. Clothiaux for his comments on the manuscript. This work was performed by the Lawrence Livermore National Laboratory under the auspices of the Department of Energy under contract W-7405-ENG-48 and was supported by the NASA High Energy Astrophysics Supporting Research and Technology Program work order W-19127.

## REFERENCES

- Arnaud, M., & Raymond, J. 1992, *ApJ*, 398, 394  
 Arnaud, M., & Rothenflug, R. 1985, *A&AS*, 60, 425  
 Arimoto, N., Matshushita, K., Ishimaru, Y., Ohashi, T., & Renzini, A. 1997, *ApJ*, 477, 128  
 Bar-Shalom, A., & Klapisch, M. 1988, *Comput. Phys. Commun.*, 50, 375  
 Beiersdorfer, P., et al. 1986, *Phys. Rev. A*, 34, 1297  
 Beiersdorfer, P., Crespo, J. R., Förster, E., Mahiri, J., & Widmann, K. 1997, *Rev. Sci. Instrum.*, 68(1), 1077  
 Beiersdorfer, P., et al. 1990, *Phys. Rev. L.*, 65, 1995  
 Beiersdorfer, P., Phillips, T. W., Wong, K. L., Marrs, R. E., & Vogel, D. A. 1992, *Phys. Rev. A*, 46, 3812  
 Beiersdorfer, P., Vogel, D. A., Reed, K., Decaux, V., Scofield, J., & Widmann, K. 1996, *Phys. Rev. A*, 53, 3974  
 Beiersdorfer, P., et al. 1988, *Phys. Rev. A*, 37, 4153  
 Beiersdorfer, P., & Wargelin, B. J. 1994, *Rev. Sci. Instrum.*, 65(1), 13  
 Bely, O., & Bely, F. 1967, *Sol. Phys.*, 2, 285  
 Bhatia, A. K., & Doschek, G. A. 1992, *At. Data Nucl. Data Tables*, 52, 1  
 Bhatia, A. K., Feldman, U., & Seely, J. F. 1985, *At. Data Nucl. Data Tables*, 32, 435  
 Blake, R. L., Chubb, T. A., Friedman, H., & Unizicker, A. E. 1965, *ApJ*, 142, 1  
 Boiko, V. A., Faenov, A. Ya., & Pikuz, S. A. 1978, *J. Quantum Spectrosc. Radiat. Transfer*, 19, 11  
 Borkowski, C. J., & Kopp, M. K. 1968, *Rev. Sci. Instrum.*, 39(10), 1515  
 Burek, A. 1976, *Space Sci. Instrum.*, 2, 53  
 Burkhalter, P. G., Dozier, D. M., Stallings, C., & Cowan, R. D. 1978, *J. Appl. Phys.*, 49, 1092  
 Chantrenne, S., Beiersdorfer, P., Cauble, R., & Schneider, M. B. 1992, *Phys. Rev. L.*, 69, 265  
 Cornille, M., Dubau, J., Faucher, P., Bely-Dubau, F., & Blanchard, C. 1994, *A&AS*, 105, 77  
 Cowan, R. D. 1981, *The Theory of Atomic Structure and Spectra* (Berkeley: UC Berkeley Press)  
 Decaux, V., Beiersdorfer, P., Kahn, S. M., & Jacobs, V. L. 1997, *ApJ*, 482, 1076  
 Decaux, V., Beiersdorfer, P., Osterheld, A., Chen, M., & Kahn, S. M. 1995, *ApJ*, 443, 464  
 Dietrich, D. D., Chandler, G. A., Fortner, R. J., Hailey, C. J., & Stewart, R. E. 1985, *Phys. Rev. Lett.*, 54, 1008  
 Drake, G. W. 1988, *Canadian J. Phys.*, 66, 586  
 Doschek, G. A., & Cowan, R. D. 1984, *ApJS*, 56, 67  
 Freeman, F. F., & Jones, B. B. 1970, *Sol. Phys.*, 15, 288  
 Garcia, J. D., & Mack, J. E. 1965, *J. Opt. Soc. Am.*, 55(6), 654  
 Hagelstein, P. L., & Jung, R. K. 1987, *At. Data Nucl. Tables*, 37, 121  
 Henke, B. L., Gullikson, E. M., & Davis, J. C. 1993, *At. Data Nucl. Tables*, 54, 181  
 Hutcheon, R. H., Pye, F. P., & Evans, K. D. 1976, *MNRAS*, 175, 489  
 Hwang, U., Mushotsky, R. F., Lowenstein, M., Markert, T. H., Fukazawa, Y., & Matsumoto, H. 1997, *ApJ*, 476, 560  
 Kahn, S. M., Seward, F. D., & Chlebowski, T. 1984, *ApJ*, 283, 286  
 Klapisch, M. 1971, *Comput. Phys. Commun.*, 2, 239  
 Levine, M. A., Marrs, R. E., Bennett, C. L., Henderson, J. R., Knapp, D. A., & Schneider, M. B. 1989, in *AIP Conf. Proc.* 188, *International Symposium on Electron Beam Ion Sources and Their Applications*, ed. A. Herschovitch (New York: AIP), 182  
 Levine, M. A., Marrs, R. E., Henderson, J. R., Knapp, D. A., & Schneider, M. B. 1988, *Phys. Scr.*, T22, 157  
 Liedahl, D. A., & Brickhouse, N. 1998, in preparation  
 Liedahl, D. A., Osterheld, A. L., & Goldstein, W. H. 1995, *ApJ*, 438, L115  
 Loulergue, M., & Nussbaumer, H. 1973, *A&A*, 24, 209  
 ———. 1975, *A&A*, 45, 125  
 Mann, J. B. 1983, *At. Data Nucl. Tables*, 29, 407  
 Markert, T. H. 1991, *Proc. SPIE*, 1549, 408  
 McKenzie, D. L., & Landecker, P. B. 1982, *ApJ*, 254, 309  
 McKenzie, D. L., Landecker, P. B., Broussard, R. M., Rugge, H. R., & Young, R. M. 1980, *ApJ*, 241, 409  
 McKenzie, D. L., Landecker, P. B., Feldman, U., & Doschek, G. A. 1985, *ApJ*, 289, 289  
 Mewe, R., Gronenschild, E. H. B. M., & van den Oord, G. H. J. 1985, *A&AS*, 62, 197  
 Mewe, R., Kaastra, J., & Liedahl, D. A. 1995, *Legacy*, 6, 16  
 Mohan, M., Sharma, R., & Eissnar, W. 1997, *ApJ*, 108, 389  
 Parkinson, J. H. 1973, *A&A*, 24, 215  
 ———. 1975, *Sol. Phys.*, 42, 183

- Phillips, K. J. H., et al. 1982, *ApJ*, 256, 774
- Phillips, K. J. H., Greer, C. J., Bhatia, A. K., & Keenan, F. P. 1996, *ApJ*, 469, L57
- Raymond, J. C. 1988, in *Hot Thin Plasmas in Astrophysics*, ed. R. Pallavicini (Dordrecht: Kluwer), 3
- Raymond, J. C., & Smith, B. W. 1986, *ApJ*, 306, 762
- Rice, J. E., et al. 1995, *Phys. Rev. A*, 51, 3551
- Rugge, H. R., & McKenzie, D. L. 1985, *ApJ*, 297, 338
- Savin, D. W., et al. 1996, *ApJ*, 470, L73
- Schmelz, J. T., Saba, J. L. R., & Strong, K. T. 1992, *ApJ*, 398, L115
- Smith, B. W., Raymond, J. C., Mann, J. B., & Cowan, R. D. 1985, *ApJ*, 298, 898
- Tyrén, F. 1938, *Z. Phys.*, 109, 314
- Vainshtein, L. A., & Safronova, U. I. 1985, *Phys. Scr.*, 31, 519
- Vedder, P. W., & Canizares, C. R. 1983, *ApJ*, 270, 666
- von Goeler, S., et al. 1982, in *Proc. Course Diagnostics for Fusion Reaction Conditions*, Vol. 1, ed. P. E. Scott (Brussels: Commission of the European Communities), 109
- Waljeski, K., Moses, D., Dere, K. P., Saba, J. L. R., Web, D. F., & Zarro, D. M. 1994, *ApJ*, 429, 909
- Wargelin, B. J., Beiersdorfer, P., & Kahn, S. M. 1993, *Phys. Rev. Lett.*, 71, 2196
- Winkler, P. F., Canizares, C. R., Clark, G. W., Markert, T. H., Kalata, K., & Schnopper, H. W. 1981, *ApJ*, 246, L27
- Zhang, H. L., Sampson, D. H., Clark, R. E., & Mann, J. B. 1987, *At. Data Nucl. Tables*, 37, 17